Chemical vapour deposition of Fe–N–C oxygen reduction catalysts with full utilization of dense Fe–N$_4$ sites

Li Jiao[1], Jingkun Li[2], Lynne LaRochelle Richard[3], Qiang Sun[3], Thomas Stracensky[3], Ershuai Liu[3], Moulay Tahar Sougrati[2], Zipeng Zhao[4], Fan Yang[5], Sichen Zhong[5], Hui Xu[5], Sanjeev Mukerjee[3], Yu Huang[4,6], David A. Cullen[7], Jae Hyung Park[8], Magali Ferrandon[8], Deborah J. Myers[8 ✉], Frédéric Jaouen[2 ✉] and Qingying Jia[3 ✉]

Replacing scarce and expensive platinum (Pt) with metal–nitrogen–carbon (M–N–C) catalysts for the oxygen reduction reaction in proton exchange membrane fuel cells has largely been impeded by the low oxygen reduction reaction activity of M–N–C due to low active site density and site utilization. Herein, we overcome these limits by implementing chemical vapour deposition to synthesize Fe–N–C by flowing iron chloride vapour over a Zn–N–C substrate at 750 °C, leading to high-temperature trans-metalation of Zn–N$_4$ sites into Fe–N$_4$ sites. Characterization by multiple techniques shows that all Fe–N$_4$ sites formed via this approach are gas-phase and electrochemically accessible. As a result, the Fe–N–C catalyst has an active site density of 1.92×10^{20} sites per gram with 100% site utilization. This catalyst delivers an unprecedented oxygen reduction reaction activity of 33 mA cm^{-2} at 0.90 V (iR-corrected; i, current; R, resistance) in a H$_2$–O$_2$ proton exchange membrane fuel cell at 1.0 bar and 80 °C.

While fuel cell electric vehicles based on proton exchange membrane fuel cells (PEMFCs) were first commercialized in 2014, the large amount of platinum in current fuel cell electric vehicles is an impediment to large-scale and sustainable deployment[1]. Platinum is mainly needed to catalyse the oxygen reduction reaction (ORR) at the cathode[2], and worldwide research efforts focus on developing ORR catalysts free of platinum group metals (PGMs). The US Department of Energy (DOE) has set a 2025 ORR activity target for PGM-free PEMFC cathodes of 44 mA cm^{-2} at 0.90 V, with 1.0 bar H$_2$ and O$_2$ (ref. [3]), comparable to the ORR activity of PGM-based electrodes.

The most active PGM-free ORR catalysts are pyrolysed metal–nitrogen–carbon (M–N–C) materials[4–10]. State-of-the-art Fe–N–C catalysts are produced by hard-[11,12] and soft-templating methods[4,7,9,13,14] derived from the original method of Yeager et al. in 1989 (ref. [15]). Key steps common to these synthetic methods are the use of catalyst precursors comprising iron, nitrogen and carbon and pyrolysis of these precursors to form the catalyst materials. The consensus reached with numerous characterization efforts is that the pyrolysis step forms Fe–N$_4$ sites[13,16–18] embedded in a graphite matrix, while the number of accessible Fe–N$_4$ sites per gram of catalyst (site density, SD$_{mass}$) correlates with the material's ORR activity in acidic electrolyte. Recently, Strasser's and Kucernak's groups developed two methods to quantify SD$_{mass}$ based on gas-phase and electrochemical adsorption, respectively[19–22]. Coupled with ORR mass activity measurements, these methods also provide the site's average ORR turnover frequency (TOF). Applying these methods

to four benchmark Fe–N–C catalysts, it was shown that the highest SD$_{mass}$ (~6×10^{19} sites per gram) and TOF (~$0.7\,e$ site^{-1} s^{-1} at 0.8 V at pH 1)[19] are approximately an order of magnitude lower than those of Pt/C (refs. [23,24]).

Increasing the TOF of PGM-free catalysts is challenging, with the most promising alternatives, such as Sn–N–C, showing a TOF similar to Fe–N–C (ref. [25]). In the absence of pathways to increase the TOF, the only other available approach to increase ORR mass activity is to increase SD$_{mass}$. This goal currently faces two challenges: (1) the parallel formation during pyrolysis of ORR-inactive or less-active Fe species[9,14,26] and Fe–N$_4$ sites and (2) the low utilization of Fe–N$_4$ sites, a considerable fraction being buried in the N-doped carbon matrix and therefore inaccessible by air[12,21]. We define two utilization subfactors, U_{Fe} and U_{FeN4}, the former being the ratio of the number of Fe–N$_4$ moieties to the total number of Fe atoms in the catalyst, and the latter, the ratio of electrochemically accessible Fe–N$_4$ moieties to all Fe–N$_4$ moieties. SD$_{mass}$ is proportional to the product of the Fe content and the overall utilization, U, where $U = U_{Fe} \times U_{FeN4}$ (Supplementary Information equation (2)). As an example of the challenge of increasing SD$_{mass}$, Shui et al.[12] showed that, due to strong Fe clustering at high Fe content, the U of their Fe–N–C catalysts dropped from ~0.4 to ~0.1 when the Fe content was increased from 0.3 to 2.8 wt%, resulting in a maximum SD$_{mass}$ of 3.4×10^{19} sites per gram. Primbs et al.[19] also showed that U_{FeN4} was in the range of 0.20–0.45 for the catalysts in their study. A synthetic approach that leads to increases in both U_{FeN4} and U_{Fe} values at higher Fe contents is therefore critical to enhancing ORR activity.

[1]Department of Chemical Engineering, Northeastern University, Boston, MA, USA. [2]Institut Charles Gerhardt Montpellier, University of Montpellier, CNRS, ENSCM, Montpellier, France. [3]Department of Chemistry and Chemical Biology, Northeastern University, Boston, MA, USA. [4]Department of Materials Science and Engineering, University of California, Los Angeles, CA, USA. [5]Giner, Newton, MA, USA. [6]California NanoSystems Institute, University of California, Los Angeles, CA, USA. [7]Center for Nanophase Materials Sciences, Oak Ridge National Laboratory, Oak Ridge, TN, USA. [8]Chemical Sciences and Engineering Division, Argonne National Laboratory, Lemont, IL, USA. ✉e-mail: dmyers@anl.gov; frederic.jaouen@umontpellier.fr; qjia@iit.edu
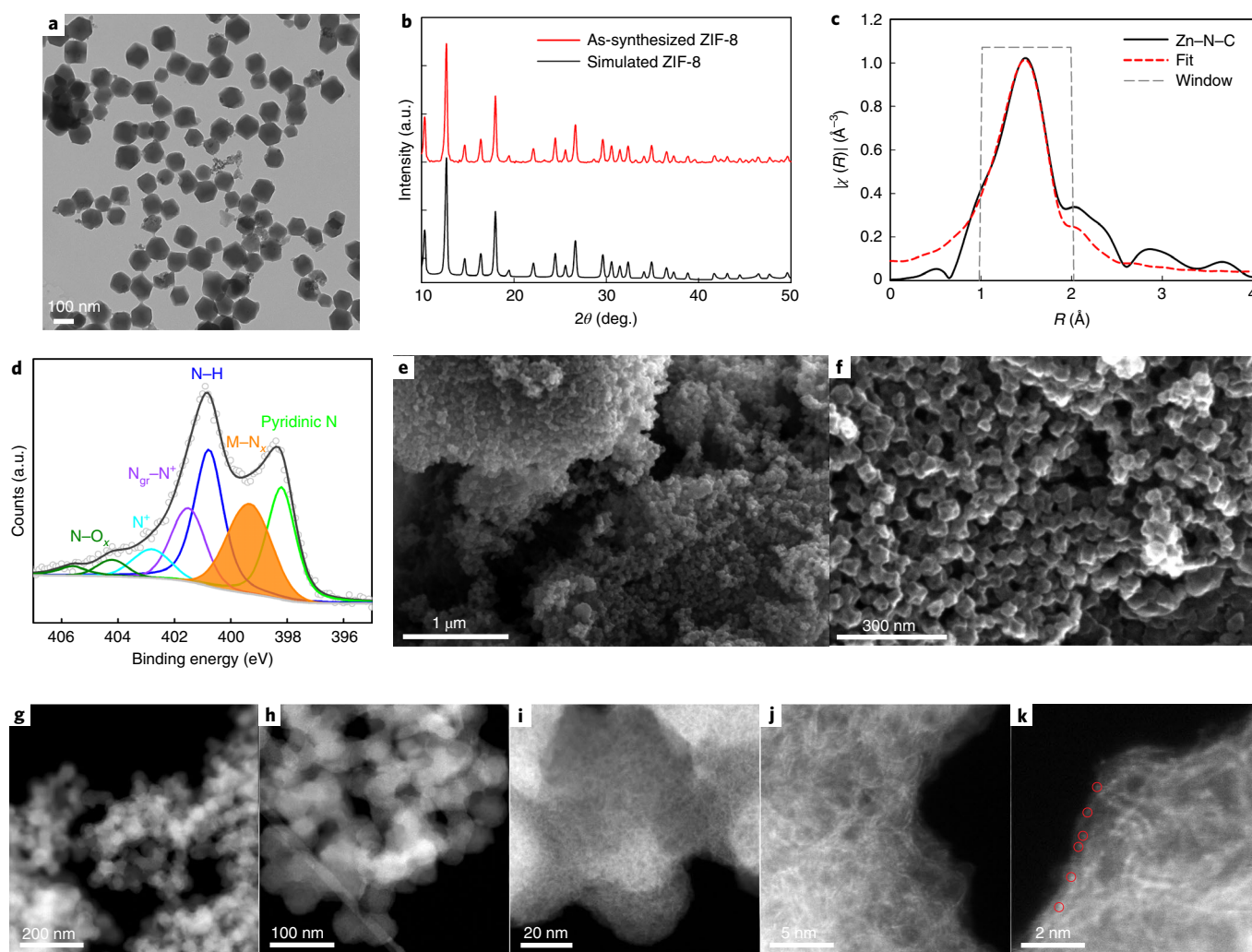
Fig. 1 | Characterization of the synthesized ZIF-8 and the ZIF-8-derived Zn–N–C substrate. a, Transmission electron microscopy (TEM) image of ZIF-8. **b**, X-ray diffraction patterns of ZIF-8 and simulated pattern (JCPDS database file 00-062-1030). θ is the angle of diffraction. **c**, Zn K-edge Fourier transform EXAFS spectrum of Zn–N–C and fit. R is interatomic distance. The indicated radial distance is not corrected for phase shift. $\chi(R)$ is the Fourier transform in the R space. **d**, Narrow-scan N_{1s} XPS of Zn–N–C, with peak assignments according to ref. [30]. N_{gr} represents graphitic nitrogen. The solid orange line represents the N bonded with metal (M-N_x). The solid black line represents the fit of the data. **e,f**, SEM images of Zn–N–C. **g–k**, AC-STEM in ADF images of Zn–N–C at various magnifications. Residual Zn atoms are circled in red to guide the eye.

Herein we implement a chemical vapour deposition (CVD) synthesis, flowing iron chloride vapour over a bed of Zn–N–C material, to preferentially form accessible Fe–N$_4$ sites with self-optimized Fe content. We show that this approach results in simultaneously high U_{Fe} (~0.9), U_{FeN4} (1) and Fe content (~2.0 wt%). Together, this results in an unprecedented SD$_{mass}$ of 1.92×10^{20} sites per gram. This catalyst exhibits an ORR activity of 44 mA cm^{-2} at 0.89 V (iR-corrected) in an H$_2$–O$_2$ PEMFC, only 0.01 V lower than the DOE 2025 target[3].

To obtain a Zn–N–C material with a high density of Zn–N$_4$ sites, we first prepared nano-crystals of a zeolitic imidazolate framework (ZIF-8) with a uniform size of ~80 nm (Fig. 1a). ZIF-8 was the sole crystalline product, as verified by X-ray diffraction (Fig. 1b). All Zn atoms have the expected tetrahedral Zn–N$_4$ structure, as confirmed by extended X-ray absorption fine structure (EXAFS; Supplementary Fig. 1 and Supplementary Table 1).

The nanosized ZIF-8 (1.0 g) was mixed with 1,10-phenanthroline (0.25 g) in ethanol/water, and the suspension was dried. The generated dry powder was homogenized via low-energy ball milling, then pyrolysed under Ar at 1,050 °C. The resulting Zn–N–C material contains 4.23 wt% N and 2.16 wt% Zn (Supplementary

Table 2a). Fitting of the Zn K-edge EXAFS spectrum identifies Zn–N$_4$ sites (Fig. 1c and Supplementary Table 1), in line with previous reports on carbonaceous materials obtained via ZIF-8 pyrolysis[27–29]. The existence of Zn–N bonds is further supported by the fit of the X-ray photoelectron spectroscopy (XPS) N$_{1s}$ spectrum (Fig. 1d), which shows a peak at ~399.5 eV, commonly assigned to the N–metal interaction[30]. The Zn–N–C has Brunauer–Emmett–Teller and microporous surface areas of 807 and 692 m^2 g^{-1}, respectively. Its high porosity is a result of the high microporosity of ZIF-8 combined with the preserved size and shape of ZIF-8 crystals upon their transformation into Zn–N–C particles (Fig. 1e,f). Single Zn atoms embedded in Zn–N–C are visualized using aberration-corrected scanning transmission electron microscopy (AC-STEM) in annular dark-field (ADF) images (Fig. 1g–k).

Anhydrous FeCl$_3$ was chosen as the Fe source due to its low boiling point, ~316 °C (ref. [31]). FeCl$_3$ (80 mg) and Zn–N–C (80 mg) were placed in a quartz tube, in two separate boats 1 cm apart, with FeCl$_3$ in the upstream boat. Pyrolysis was performed at 650 °C, 750 °C, 900 °C or 1,000 °C for three hours, followed by cooling to room temperature under Ar flow. The ORR activities of the powders collected
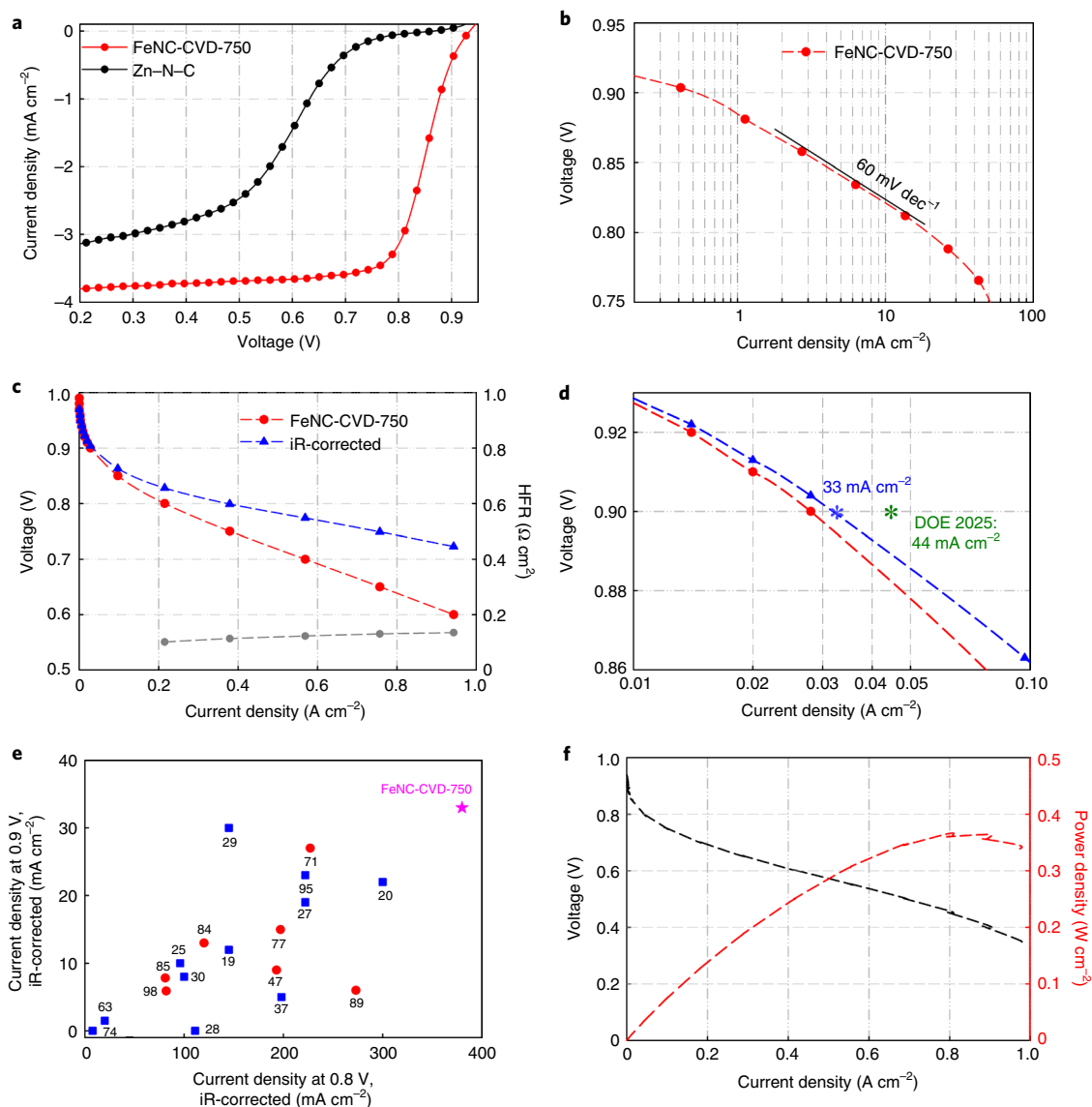
Fig. 2 | ORR activity and performance of FeNC-CVD-750. a, Steady-state RDE polarization curves in O_2-saturated 0.5 M H_2SO_4 at room temperature, 900 r.p.m., 20 mV potential steps from 0.05 to 0.95 V (all potentials given versus reversible hydrogen electrode (RHE)) and a 25 s potential hold at each step. Catalyst loading, 800 μg cm^{-2}. **b**, Tafel plot derived from the ORR polarization curve of FeNC-CVD-750 displayed in **a**. **c**, H_2-O_2 PEMFC polarization curves with and without iR-correction. Cathode, ~6.0 mg$_{cat}$ cm^{-2}; anode, 0.3 mg$_{Pt}$ cm^{-2} Pt/C; Nafion 212; 200 ml H_2 min^{-1} and 1,000 ml O_2 min^{-1} feed, 100% relative humidity (RH), 1.0 bar partial pressure H_2 and O_2, 80 °C, electrode area 5 cm^2. The grey dotted curve represents the high-frequency resistance (HFR). **d**, Tafel plots derived from the ORR polarization curves displayed in **c**. **e**, Comparison of the H_2-O_2 PEMFC activity at 0.9 V (iR-corrected) and 0.8 V (iR-corrected) of FeNC-CVD-750 with literature values. The literature data are labelled with numbers that represent the reference number in Osmieri et al.[34]. The data points in blue were collected at 100% RH, 1.0 bar partial pressure of H_2 and O_2, and 80 °C, whereas the data points in red were collected at 100% RH, 2.0 bar partial pressure of H_2 and O_2, and 80 °C. **f**, The H_2-air PEMFC polarization curve and power density without iR-correction for the MEA acquired after the H_2-O_2 polarization curves; 500 ml min^{-1} H_2 and 2,000 ml min^{-1} air, 100% RH, 1.0 bar H_2 and air partial pressure, and 80 °C.

from the downstream boat (labelled as FeNC-CVD-T, where T represents the pyrolysis temperature) were measured using a rotating disk electrode (RDE). FeNC-CVD-750 exhibited the highest ORR activity (Supplementary Fig. 2) with a half-wave potential of 0.85 V (Fig. 2a) and kinetic current density, j_k, of 20 mA cm^{-2} (25 mA per milligram catalyst (mg$_{cat}$$^{-1}$)) at 0.80 V (Fig. 2b). This activity is among the highest reported for Fe–N–C catalysts[19,20].

The FeNC-CVD-750-containing cathode was then evaluated in a H_2–O_2 PEMFC for three polarization scans, followed by evaluation in H_2–air. A current density of 44 mA cm^{-2} was reached at 0.89 V (iR-corrected) during the first scan (increasing current) in H_2–O_2, only 0.01 V lower than the DOE 2025 target[3]

(Fig. 2c,d). The current densities at 0.9 V (iR-corrected) and 0.8 V (iR-corrected) are 33 and 380 mA cm^{-2}, respectively, exceeding the values previously reached by PGM-free catalysts under similar conditions (Fig. 2e). The current density at 0.9 V (iR-corrected) dropped to 22 and 18 mA cm^{-2} on the second and third scans, respectively (Supplementary Fig. 3), illustrating the poor stability of FeNC-CVD-750 in the PEMFC environment, similar to all highly active Fe–N–C catalysts[32,33]. A maximum power density of 0.37 W cm^{-2} was obtained in H_2–air (Fig. 2f), among the highest values reported for PGM-free cathodes to date[34] despite substantial ORR activity loss during the H_2–O_2 PEMFC scans performed prior to the H_2–air evaluation.
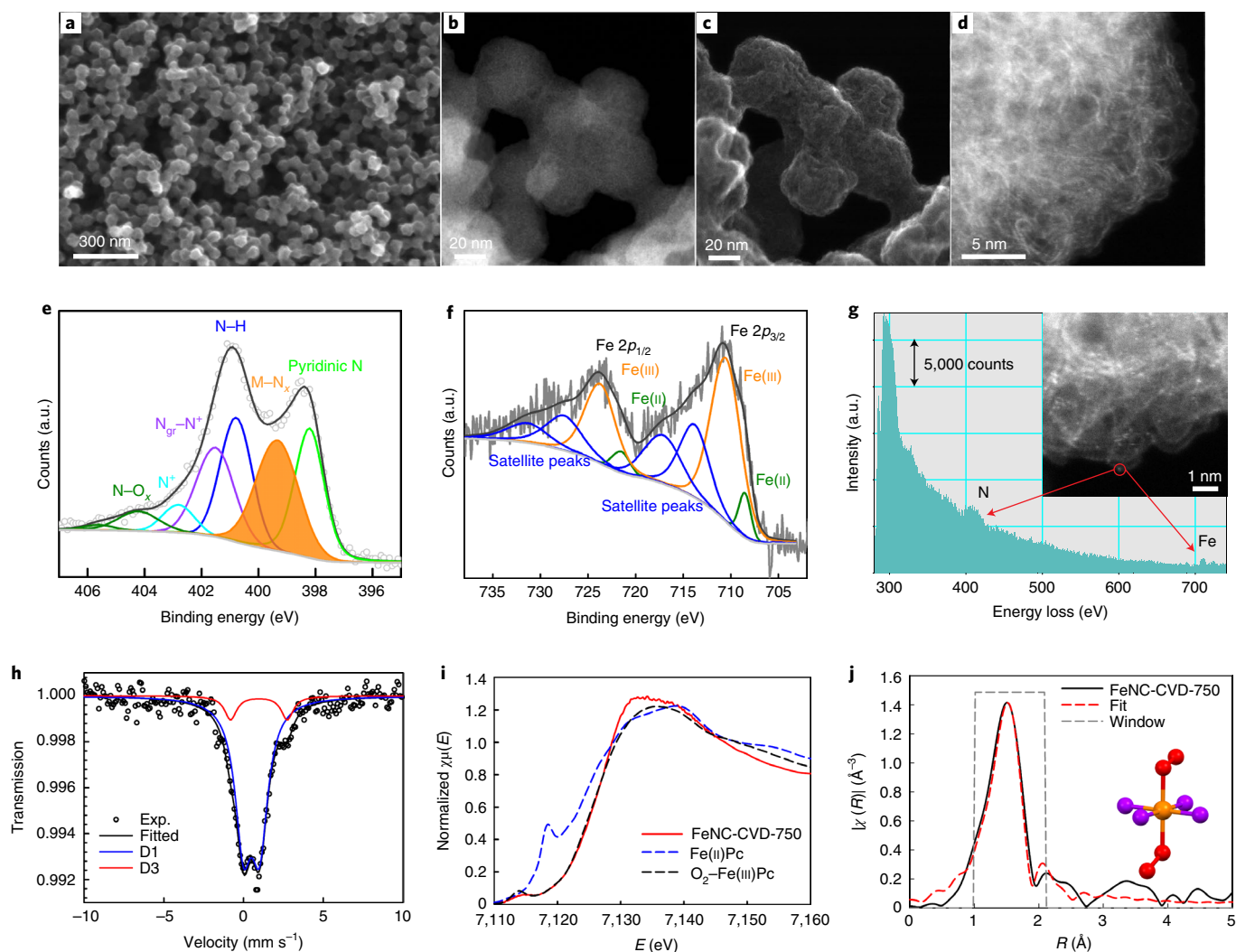
Fig. 3 | Characterization of FeNC-CVD-750. a, SEM image. **b,c**, ADF-STEM (**b**) and secondary-electron STEM (**c**) image pair. **d**, Atomic-resolution ADF-STEM image. **e**, High-resolution N_{1s} XPS spectrum. The assignments of N species follow a recent work[30]. The solid orange line represents the N bonded with metal ($M-N_x$). The solid black line represents the fit to the data. **f**, High-resolution XPS Fe_{2p} spectrum fitted with Fe(III) (90%) and Fe(II) (10%) species. **g**, Electron energy-loss spectroscopy showing the N K edge and Fe L edge acquired from a single atom (bright dot in the inset in which an atomic-resolution AC-STEM image is displayed). **h**, The ^{57}Fe Mössbauer spectrum measured at 5 K fitted with D1 (89%) and D3 (11%). Exp., experiment. **i**, Ex situ XANES spectrum together with those of Fe(II)Pc and O_2-Fe(III)Pc standards for comparison. E is the energy of the X-ray beam. $\chi\mu(E)$ represents the XANES spectrum. **j**, Ex situ Fe K-edge Fourier transform EXAFS spectrum and its fitting, with the O_2-Fe(III)$-N_4$ model presented in the inset, wherein the orange, red and purple balls represent Fe, O and N atoms, respectively. The fitting results are listed in Supplementary Table 4.

To understand the source of its exceptional ORR activity, FeNC-CVD-750 was characterized using multiple techniques. A representative scanning electron microscopy (SEM) image (Fig. 3a) shows a similar morphology to Zn–N–C (Fig. 1f) while ADF-STEM and secondary-electron STEM images show no evidence of metal clusters (Fig. 3b–d). The X-ray diffraction pattern (Supplementary Fig. 4a), C and N contents (Supplementary Table 2a) and XPS N_{1s} spectrum (Fig. 3e and Supplementary Fig. 4b) of FeNC-CVD-750 are also similar to those of Zn–N–C. The XPS Fe_{2p} spectrum can be well fitted with 90% Fe(III) and 10% Fe(II) species (Fig. 3f). Abundant bright dots are seen in the ADF-STEM image (Fig. 3g, inset), for which the electron energy-loss spectroscopy spectrum shows the close proximity of single Fe and N atoms (Fig. 3g and Supplementary Fig. 5). This demonstrates the presence of abundant Fe–N_x moieties in FeNC-CVD-750. In addition, the uniform distribution of Fe and fluorine (ADF-STEM images of the membrane electrode assembly (MEA)'s cathode, Supplementary

Fig. 6) shows an extended interface between the ionomeric and catalytic phases.

The presence of Fe–N_x moieties in FeNC-CVD-750 is also supported by ^{57}Fe Mössbauer spectra collected at 5 K (Supplementary Note 1 on the importance of low-temperature measurement). Two doublets, labelled D1 and D3, representing 89% and 11% of the absorption area, respectively (Fig. 3h and Supplementary Table 3), were identified. D1 (with a quadrupole splitting of 1.02 mm s^{-1}) has been repeatedly observed in Fe–N–C materials, but has only recently been identified as an O_2-Fe(III)$-N_4-C_{12}$ moiety, a porphyrinic site structure with an O_2 (or OH$^-$) ligand adsorbed on Fe (refs. [13,17]). The ferric state and presence of an oxygenated axial ligand suggest that all D1 sites are gas-phase accessible. Ex situ Fe K-edge X-ray absorption near edge structure (XANES; Fig. 3i) and EXAFS (Fig. 3j and Supplementary Table 4) analysis further confirms that O_2-Fe(III)$-N_4$ is the dominant Fe site in FeNC-CVD-750. We note the absence of the doublet with isomer shift similar to that for D1
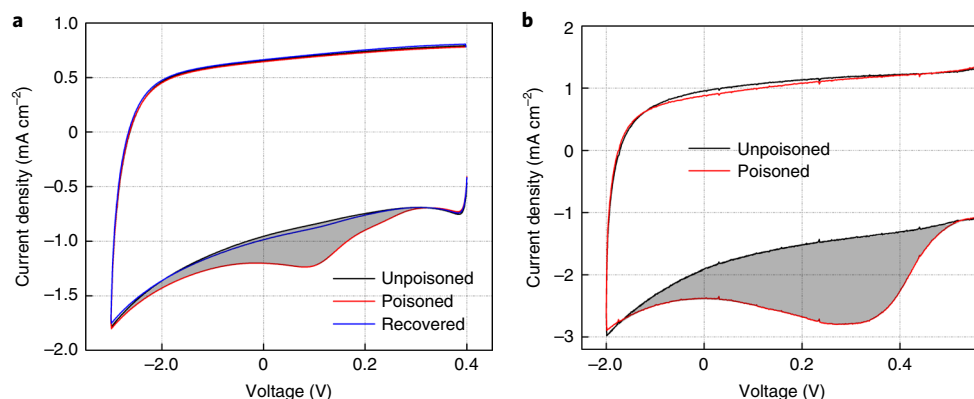
Fig. 4 | In situ evaluation of the SD$_{mass}$ of FeNC-CVD-750. a, Nitrite stripping voltammetry in N$_2$-saturated 0.5 M acetate electrolyte buffer (pH 5.2) with a catalyst loading of 270 µg cm^{-2} and a scan rate of 10 mV s^{-1}. **b**, NO stripping voltammetry in N$_2$-saturated 0.5 M H$_2$SO$_4$ with a catalyst loading of 600 µg cm^{-2} and a scan rate of 10 mV s^{-1}. The grey shading represents the excess current associated with the reductive stripping of nitrite.

but with a higher quadrupole splitting value of 2.3–2.7 mm s^{-1}, labelled D2 in the Fe–N–C literature[17,18,35,36]. D2 was identified to be an Fe(II)–N$_4$ site[13,17], with oxidation and spin state unchanged with electrochemical potential[37,38]. This suggests that the CVD synthesis selectively forms gas-phase-accessible Fe–N$_4$ sites. D3 can be unambiguously assigned to a high-spin Fe^{2+} species, due to its high isomer shift of 1.0 mm s^{-1}.

Previously reported Fe–N–C catalysts showing a doublet with isomer shift and quadrupole splitting values similar to those of D3 were synthesized using iron chloride precursors (Supplementary Table 5)[27,39]. Among the various ferrous chlorides, only FeCl$_2$·4H$_2$O leads to a doublet with isomer shift and quadrupole splitting values matching those of D3 (Supplementary Table 6)[40,41]. The residual presence of FeCl$_2$ after FeCl$_3$ CVD is independently supported by the identification, after temperature-programmed reaction analysis, of a hydrated FeCl$_2$ deposit downstream of the FeCl$_3$ and Zn–N–C (Supplementary Fig. 8) and is expected since FeCl$_3$ decomposition is initiated at 300 °C (ref. [42]). Together, these observations strongly support the assignment of the observed D3 to FeCl$_2$·4H$_2$O (Supplementary Notes 2 and 3 for details). The assignments of D1 and D3 quantitatively agree with the XPS results of ~90% Fe(III) and ~10% Fe(II) and, importantly, imply U_{Fe} of ~0.9 (D1 relative percent), U_{FeN4} of 1 and a high SD$_{mass}$ of 1.94 × 10^{20} sites per gram. Combined cyclic voltammetry (CV) and in situ XANES further showed that all the D1 sites in FeNC-CVD-750 undergo a reversible Fe(III)/Fe(II) redox transition at ~0.66 V (Supplementary Fig. 9 and Supplementary Note 4). The number of redox-active Fe sites derived from the charge of the redox peak is 2.0 × 10^{20} sites per gram, similar to the SD$_{mass}$ derived from Mössbauer, suggesting that the D1 sites in FeNC-CVD-750 are both gas and proton accessible, and contribute largely to the redox signal in the CV images.

The U and SD$_{mass}$ values of FeNC-CVD-750 were further determined by the electrochemical stripping of NO formed by exposure to aqueous nitrite[19,22] and by exposure to gaseous NO. These methods are based on the formation of the strong NO–Fe adduct and the estimation of SD$_{mass}$ based on the electric charge needed to reduce NO, represented by the grey areas in Fig. 4a,b. In contrast to the initial assumption of complete five-electron electroreduction of NO to ammonia[22], we assumed that only three electrons were transferred, forming hydroxylamine (Supplementary Information equation (6)), based on a recent report[43] showing that an Fe–N–C catalyst containing only Fe–N$_4$ sites selectively reduced NO to hydroxylamine (Supplementary Note 5). The SD$_{mass}$ determined by stripping of gas-phase adsorbed NO is 1.9 × 10^{20} sites per gram, in agreement with that obtained by Mössbauer. This value is at least three times higher than that achieved hitherto[12,19,44]. Finally, the SD$_{mass}$ estimated

by stripping of NO formed from nitrite (SD$_{mass}$(NO$_2^-$)) is 1.0 × 10^{20} sites per gram, about half of those determined by other methods. This agrees with the benchmarking study[19], where SD$_{mass}$(NO$_2^-$) values were two to eight times lower than those derived from CO cryo-chemisorption, and it was proposed that SD$_{mass}$(NO$_2^-$) gives the lower bound of the SD$_{mass}$ of Fe–N–C catalysts.

The utilization factor, U, of ~0.9 for FeNC-CVD-750 can be derived from the average SD$_{mass}$ of 1.92 × 10^{20} sites per gram (Supplementary Information equation (2)). It is comparable to the highest reported U for Fe–N–C catalysts. However, those catalysts contained both D1 and D2 species, and the U values were obtained by dividing the number of CO-accessible Fe–N$_4$ sites solely by the number of D1 sites[21]. This indicates that the high U for FeNC-CVD-750 is realized through CVD synthesis, which selectively forms gas-phase-accessible Fe–N$_4$ sites (D1). Therefore, the negative correlation between U and the Fe content and the limited site accessibility encountered with traditional Fe–N–C catalyst synthesis methods are alleviated by using the CVD method.

The ORR TOF (0.8 V) in FeNC-CVD-750 is 0.8 e site^{-1} s^{-1}, as derived from j_k (0.8 V) in 0.5 M H$_2$SO$_4$ and from the average SD$_{mass}$ of 1.92 × 10^{20} sites per gram (Supplementary Information equation (8)). This TOF is comparable to those derived using CO cryo-chemisorption (0.2–1.5 e site^{-1} s^{-1})[19,20], indicating that the high activity of FeNC-CVD-750 relative to other Fe–N–C catalysts results from its high SD$_{mass}$ rather than an increase in TOF. This conclusion is confirmed by comparing the SD$_{mass}$(NO$_2^-$) and TOF(NO$_2^-$) of FeNC-CVD-750 with those of previous Fe–N–C catalysts (Supplementary Note 5 and Supplementary Fig. 11).

Next, we discuss the site formation mechanism with the CVD approach and how it leads to high site utilization. The double-layer capacitance of Zn–N–C and FeNC-CVD-750 is ~0.16 and 0.36 F mg^{-1}, respectively, as derived from CV (Supplementary Fig. 9a) at 0.3 V. Assuming a specific capacitance of the carbon surface of 204 mF m^{-2} (ref. [13]), this corresponds to electrochemical surface areas of ~812 and ~1,800 m^2 g^{-1}, respectively. These values agree with the Brunauer–Emmett–Teller areas of 807 and 1,593 m^2 g^{-1}, respectively. The pore distribution analysis shows a substantial increase in the abundance of both micropores (<2 nm) and mesopores after the CVD (Supplementary Fig. 12). This dramatic enhancement in electrochemical surface area did not occur when the CVD was performed at 650 °C (Supplementary Fig. 13).

Meanwhile, the Zn content in FeNC-CVD-650 is much higher than that in FeNC-CVD-750 (1.05 and 0.12 wt%, Supplementary Table 2a), and akin to the Zn content of Zn–N–C (2.16 wt%). This suggests an inter-relation between the changes in electrochemical surface area and the Fe and Zn contents resulting from the CVD.
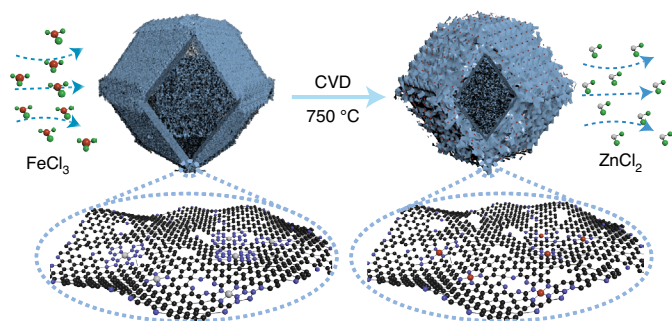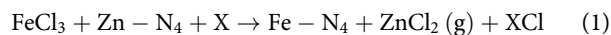
Fig. 5 | High-temperature trans-metalation. Synthesis of FeNC-CVD-750 via $FeCl_3$ CVD. Red, green, grey, purple and black balls represent Fe, Cl, Zn, N and C atoms, respectively.

Subjecting Zn–N–C to the same pyrolysis conditions, but in the absence of $FeCl_3$ vapour, led to an unmodified Zn content up to 900 °C (Supplementary Table 2b). This, and the previously described temperature effect in the presence of $FeCl_3$, demonstrate that the removal of Zn requires the presence of $FeCl_3$ and high temperature (>650 °C). We further make four important observations: (1) the low residual content of Zn in FeNC-CVD-750 is in the form of Zn–N_4 sites (Supplementary Fig. 14); (2) $ZnCl_2$ has a boiling point of 732 °C, matching the temperature range where the Zn content drastically decreases after CVD (650–750 °C, Supplementary Table 2a); (3) the decrease in Zn content is quantitatively accompanied by a similar increase in Fe content (Supplementary Table 2a); and (4) this occurs without notable change in the N-metal XPS peak (Supplementary Fig. 4b). These observations lead us to propose that the Fe–N_4 sites are formed via high-temperature trans-metalation that involves the exchange of Fe and Zn between Zn–N_4 and $FeCl_3$ during the CVD at 750 °C (Fig. 5):

$$FeCl_3 + Zn - N_4 + X \rightarrow Fe - N_4 + ZnCl_2 \text{ (g)} + XCl \quad (1)$$

where X represents elements such as H and Cl that can form a compound with an additional Cl. This high-temperature trans-metalation mechanism is further supported by the observation of $ZnCl_2$ and XCl vapour via mass spectrometry during the temperature-programmed reaction of Zn–N–C and $FeCl_3$ (Supplementary Note 6 and Supplementary Fig. 15).

A low-temperature trans-metalation mechanism was recently proposed by Fellinger and coworkers to account for the formation of Fe–N_4 sites upon heating to only 170 °C, a catalyst precursor comprising iron chlorides and a Zn–N–C with Zn–N_4 sites[27,45]. While the formation of Fe–N_4 sites was supported by the presence of the D1 signal in their Mössbauer spectrum, around 50% of the Fe was in the form of oxides, and the ORR activity (a half-wave potential of ~0.7 V) was low[27]. We therefore propose that the formation of $ZnCl_2$ vapour is essential to selectively promote and complete the trans-metalation process, which rationalizes the optimized temperature of 750 °C for the CVD, just above the boiling point of $ZnCl_2$. This relatively low temperature allows the high retention of N in Zn–N–C, while the N content drops precipitously above 900 °C (Supplementary Table 2a). The latter effect has been regarded as one key factor limiting the Fe–N_4 site density[7,9]. Therefore, the M–N_4 sites are better preserved in the synthesis of FeNC-CVD-750 at a temperature that is ~200 °C lower than that previously used for Fe–N–C synthesis.

High-temperature trans-metalation also explains the full utilization of Fe–N_4 sites in FeNC-CVD-750. With this mechanism, the sites are formed at locations where the Zn–N_4 sites are accessible by $FeCl_3$ vapour, followed by the departure of the generated $ZnCl_2$

vapour from these locations (Fig. 5). $FeCl_3$ is a known intercalant of graphite, leading to well-defined $FeCl_3$–graphite intercalation compounds[46]. This implies that $FeCl_3$ may have the ability to reach Zn–N_4 sites that are not initially gas-phase accessible in Zn–N–C. The formation of $ZnCl_2$ (g) in the interlayers of graphitic crystallites via the high-temperature trans-metalation reaction may then have resulted in partial exfoliation, exposing all Fe–N_4 sites to the gas phase. Exfoliation of graphite via the calcination or pyrolysis of various graphite intercalation compounds (including $FeCl_3$–graphite intercalation compound) has been reported recently[47,48]. This site formation mechanism explains the experimental observation of inter-related enhancement of porosity during CVD of Zn–N–C at 750 °C, increased Fe content and decreased Zn content. The Fe–N_4 sites formed via high-temperature trans-metalation are therefore readily accessible by air.

In conclusion, although full utilization of active sites has long been conceived as a unique advantage of single-atom catalysts, here it has been realized in Fe–N–C catalysts by resorting to a dual-step synthesis, involving first the synthesis of Zn–N–C with Zn–N_4 sites, with subsequent reaction with $FeCl_3$ (g). The present method has two essential advantages compared to previous synthesis approaches: (1) the Fe–N_4 sites are formed at a lower temperature, retaining the higher N content needed for high site density, and (2) the Fe–N_4 sites are naturally accessible by gas, leading to high utilization. Consequently, the FeNC-CVD-750 catalyst has a high SD_{mass} and ORR performance in H_2–O_2 PEMFCs. It is also a model catalyst containing only one type of iron active site. Therefore, model catalyst and practical catalyst for the ORR are combined in a single entity using the CVD approach.

Online content

Any methods, additional references, Nature Research reporting summaries, source data, extended data, supplementary information, acknowledgements, peer review information; details of author contributions and competing interests; and statements of data and code availability are available at https://doi.org/10.1038/s41563-021-01030-2.

References

1. Thompson, S. T. & Papageorgopoulos, D. Platinum group metal-free catalysts boost cost competitiveness of fuel cell vehicles. *Nat. Catal.* **2**, 558–561 (2019).
2. Thompson, S. T. et al. Direct hydrogen fuel cell electric vehicle cost analysis: system and high-volume manufacturing description, validation, and outlook. *J. Power Sources* **399**, 304–313 (2018).
3. Thompson, S. T. et al. ElectroCat: DOE's approach to PGM-free catalyst and electrode R&D. *Solid State Ion.* **319**, 68–76 (2018).
4. Chung, H. T. et al. Direct atomic-level insight into the active sites of a high-performance PGM-free ORR catalyst. *Science* **357**, 479–484 (2017).
5. Li, J. et al. Atomically dispersed manganese catalysts for oxygen reduction in proton-exchange membrane fuel cells. *Nat. Catal.* **1**, 935–945 (2018).
6. Zitolo, A. et al. Identification of catalytic sites in cobalt-nitrogen-carbon materials for the oxygen reduction reaction. *Nat. Commun.* **8**, 957 (2017).
7. Zhang, H. et al. Single atomic iron catalysts for oxygen reduction in acidic media: particle size control and thermal activation. *J. Am. Chem. Soc.* **139**, 14143–14149 (2017).
8. Lefèvre, M., Proietti, E., Jaouen, F. & Dodelet, J.-P. Iron-based catalysts with improved oxygen reduction activity in polymer electrolyte fuel cells. *Science* **324**, 71–74 (2009).
9. Proietti, E. et al. Iron-based cathode catalyst with enhanced power density in polymer electrolyte membrane fuel cells. *Nat. Commun.* **2**, 416 (2011).
10. Banham, D. et al. Critical advancements in achieving high power and stable nonprecious metal catalyst–based MEAs for real-world proton exchange membrane fuel cell applications. *Sci. Adv.* **4**, eaar7180 (2018).
11. Serov, A. et al. Nano-structured non-platinum catalysts for automotive fuel cell application. *Nano Energy* **16**, 293–300 (2015).
12. Wan, X. et al. Fe–N–C electrocatalyst with dense active sites and efficient mass transport for high-performance proton exchange membrane fuel cells. *Nat. Catal.* **2**, 259–268 (2019).

13. Li, J. et al. Structural and mechanistic basis for the high activity of Fe-N-C catalysts toward oxygen reduction. *Energy Environ. Sci.* **9**, 2418–2432 (2016).

14. Zhang, H. et al. High-performance fuel cell cathodes exclusively containing atomically dispersed iron active sites. *Energy Environ. Sci.* **12**, 2548–2558 (2019).

15. Gupta, S., Tryk, D., Bae, I., Aldred, W. & Yeager, E. Heat-treated polyacrylonitrile-based catalysts for oxygen electroreduction. *J. Appl. Electrochem.* **19**, 19–27 (1989).

16. Li, J. et al. Evolution pathway from iron compounds to $Fe_1(II)–N_4$ sites through gas-phase iron during pyrolysis. *J. Am. Chem. Soc.* **142**, 1417–1423 (2020).

17. Mineva, T. et al. Understanding active sites in pyrolyzed Fe–N–C catalysts for fuel cell cathodes by bridging density functional theory calculations and [57]Fe Mössbauer spectroscopy. *ACS Catal.* **9**, 9359–9371 (2019).

18. Zitolo, A. et al. Identification of catalytic sites for oxygen reduction in iron- and nitrogen-doped graphene materials. *Nat. Mater.* **14**, 937–942 (2015).

19. Primbs, M. et al. Establishing reactivity descriptors for platinum group metal (PGM)-free Fe–N–C catalysts for PEM fuel cells. *Energy Environ. Sci.* **13**, 2480–2500 (2020).

20. Sahraie, N. R. et al. Quantifying the density and utilization of active sites in non-precious metal oxygen electroreduction catalysts. *Nat. Commun.* **6**, 8618 (2015).

21. Leonard, N. D. et al. Deconvolution of utilization, site density, and turnover frequency of Fe–nitrogen–carbon oxygen reduction reaction catalysts prepared with secondary N-precursors. *ACS Catal.* **8**, 1640–1647 (2018).

22. Malko, D., Kucernak, A. & Lopes, T. In situ electrochemical quantification of active sites in Fe–N/C non-precious metal catalysts. *Nat. Commun.* **7**, 13285 (2016).

23. Paulus, U. A. et al. Oxygen reduction on high surface area Pt-based alloy catalysts in comparison to well defined smooth bulk alloy electrodes. *Electrochim. Acta* **47**, 3787–3798 (2002).

24. Gasteiger, H. A., Kocha, S. S., Sompalli, B. & Wagner, F. T. Activity benchmarks and requirements for Pt, Pt-alloy, and non-Pt oxygen reduction catalysts for PEMFCs. *Appl. Catal. B Environ.* **56**, 9–35 (2005).

25. Luo, F. et al. P-block single-metal-site tin/nitrogen-doped carbon fuel cell cathode catalyst for oxygen reduction reaction. *Nat. Mater.* **19**, 1215–1223 (2020).

26. Jia, Q. et al. Spectroscopic insights into the nature of active sites in iron–nitrogen–carbon electrocatalysts for oxygen reduction in acid. *Nano Energy* **29**, 65–82 (2016).

27. Menga, D. et al. Active-site imprinting: preparation of Fe–N–C catalysts from zinc ion–templated ionothermal nitrogen-doped carbons. *Adv. Energy Mater.* **9**, 1902412 (2019).

28. Li, J. et al. Volcano trend in electrocatalytic CO_2 reduction activity over atomically dispersed metal sites on nitrogen-doped carbon. *ACS Catal.* **9**, 10426–10439 (2019).

29. Wang, Q. et al. Evolution of Zn(II) single atom catalyst sites during the pyrolysis-induced transformation of ZIF-8 to N-doped carbons. *Sci. Bull.* **65**, 1743–1751 (2020).

30. Artyushkova, K. Misconceptions in interpretation of nitrogen chemistry from X-ray photoelectron spectra. *J. Vac. Sci. Technol. A* **38**, 031002 (2020).

31. Rustad, D. S. & Gregory, N. W. Vapor pressure of iron(III) chloride. *J. Chem. Eng. Data* **28**, 151–155 (1983).

32. Shao, Y., Dodelet, J.-P., Wu, G. & Zelenay, P. PGM-free cathode catalysts for PEM fuel cells: a mini-review on stability challenges. *Adv. Mater.* **31**, 1807615 (2019).

33. Osmieri, L., Cullen, D. A., Chung, H. T., Ahluwalia, R. K. & Neyerlin, K. C. Durability evaluation of a Fe–N–C catalyst in polymer electrolyte fuel cell environment via accelerated stress tests. *Nano Energy* **78**, 105209 (2020).

34. Osmieri, L. et al. Status and challenges for the application of platinum group metal-free catalysts in proton-exchange membrane fuel cells. *Curr. Opin. Electrochem.* **25**, 100627 (2021).

35. Kramm, U. I., Ni, L. & Wagner, S. [57]Fe Mössbauer spectroscopy characterization of electrocatalysts. *Adv. Mater.* **31**, 1805623 (2019).

36. Kramm, U. I. et al. Structure of the catalytic sites in Fe/N/C-catalysts for O_2-reduction in PEM fuel cells. *Phys. Chem. Chem. Phys.* **14**, 11673–11688 (2012).

37. Li, J. et al. Identification of durable and non-durable FeN_x sites in Fe–N–C materials for proton exchange membrane fuel cells. *Nat. Catal.* **4**, 10–19 (2021).

38. Zelenay, P. *ElectroCat (Electrocatalysis Consortium)* Report No. LA-UR-20-24045 (Los Alamos National Laboratory, 2020).

39. Ferrandon, M. et al. Multitechnique characterization of a polyaniline–iron–carbon oxygen reduction catalyst. *J. Phys. Chem. C* **116**, 16001–16013 (2012).

40. Dészi, I., Ouseph, P. J. & Thomas, P. M. Mössbauer study of $FeCl_2·6H_2O$ and its decomposition product. *Chem. Phys. Lett.* **9**, 390–392 (1971).

41. DeBenedetti, S., Lang, G. & Ingalls, R. Electric quadrupole splitting and the nuclear volume effect in the ions of Fe^{57}. *Phys. Rev. Lett.* **6**, 60–62 (1961).

42. Bach, R. D., Shobe, D. S., Schlegel, H. B. & Nagel, C. J. Thermochemistry of iron chlorides and their positive and negative ions. *J. Phys. Chem.* **100**, 8770–8776 (1996).

43. Kim, D. H. et al. Selective electrochemical reduction of nitric oxide to hydroxylamine by atomically dispersed iron catalyst. *Nat. Commun.* **12**, 1856 (2021).

44. Luo, F. et al. Accurate evaluation of active-site density (SD) and turnover frequency (TOF) of PGM-free metal–nitrogen-doped carbon (MNC) electrocatalysts using CO cryo adsorption. *ACS Catal.* **9**, 4841–4852 (2019).

45. Mehmood, A. et al. Facile metal coordination of active site imprinted nitrogen doped carbons for the conservative preparation of non-noble metal oxygen reduction electrocatalysts. *Adv. Energy Mater.* **8**, 1701771 (2018).

46. Hwang, D.-M. D. in *Graphite Intercalation Compounds I: Structure and Dynamics* (eds Zabel, H. & Solin, S.) 247–281 (Springer, 1990).

47. Zhang, B., Song, J., Yang, G. & Han, B. Large-scale production of high-quality graphene using glucose and ferric chloride. *Chem. Sci.* **5**, 4656–4660 (2014).

48. Lutfullin, M. A., Shornikova, O. N., Sorokina, N. E. & Avdeev, V. V. Interaction of $FeCl_3$-intercalated graphite with intercalants of different strengths. *Inorg. Mater.* **50**, 29–34 (2014).

Methods

Chemicals. Zinc nitrate hexahydrate ($Zn(NO_3)_2 \cdot 6H_2O$, ≥99.0%), 2-methylimidazole (99%), methanol solution, zinc phthalocyanine (Zn(II) Pc, 97%), 1,10-phenanthroline monohydrate, ethanol solution, anhydrous iron(III) chloride ($FeCl_3$, 99%), iron(II) phthalocyanine (Fe(II)Pc, 95%), iron(III) phthalocyanine-tetrasulfonic acid (Fe(III)Pc–O_2, 80%), sodium acetate (99%), glacial acetic acid (99.8%), sodium nitrite and sulfuric acid (H_2SO_4, 95–97%, ppt grade) were all purchased from Sigma-Aldrich. All aqueous solutions were prepared using deionized water (18.2 MΩ cm) obtained from an ultra-pure purification system (Aqua Solutions).

Synthesis of zinc ZIF-8. A 200 ml homogeneous 0.1 M $Zn(NO_3)_2 \cdot 6H_2O$ methanol solution was added to 200 ml 0.4 M 2-methylimidazole methanol solution under magnetic stirring for one hour at room temperature. The suspension was collected and washed by centrifugation using methanol three times, and then dried at 40 °C in a vacuum oven overnight.

Synthesis of Zn–N–C. First, 1.0 g ZIF-8 and 0.25 g 1,10-phenanthroline were dispersed in a solution of ethanol and deionized water with a volume ratio of 2:1. The mixture was magnetically stirred for two hours and then dried at 80 °C in a vacuum oven overnight. The dry powders were ball milled for 3 h in a plastic container with five plastic balls with a diameter of 0.25 inch. The collected powders were pyrolysed under Ar at 1,050 °C for one hour after reaching 1,050 °C with a ramping rate of 5 °C per minute, followed by cooling down naturally to room temperature. The powders collected were labelled as Zn–N–C and were used for the non-contact pyrolysis.

CVD. For each CVD experiment, 80 mg of anhydrous $FeCl_3$ was placed in a boat in a tube upstream of the gas flow; 80 mg of Zn–N–C with a volume of 0.45 cm^{-3} was placed evenly in another boat with a dimension of 6 × 1 cm^2 in the form of a thin layer. The thickness of the Zn–N–C substrate was thus estimated as ~0.075 cm. There was a 1 cm gap between the two boats, of which one end was mechanically cut off to allow unblocked gas flow. The furnace was heated up to a variety of temperatures with a ramping rate of 25 °C per minute, and then the temperature was held at a target temperature (T) for three hours, followed by cooling down to room temperature naturally. The furnace was continuously flowed with Ar gas with a flow rate of 0.65 l min^{-1} during the heating and cooling. The powders were then collected from the Zn–N–C boat, and subject to magnetic purification by slowly moving a small magnet ~0.5 cm above to remove Fe nanoparticles. The purified powders were labelled FeNC-CVD-T. The powders were stored in a vacuum desiccator before being subject to RDE and PEMFC evaluations.

Electrochemical characterization—RDE. The catalyst powders were deposited on a glassy carbon working electrode. Catalyst inks were prepared by dispersing 10 mg of the catalyst powder in a mixture of Millipore water (36.5 µl, 18.2 MΩ cm) and ethanol (300 µl, Sigma-Aldrich, 99.8%), into which 5 wt% Nafion solution (108.5 µl, Sigma-Aldrich) was added as a binder phase. The resulting mixture was sonicated for 60 min in an ice bath, and then an aliquot of 8.8 µl was drop-cast onto the glassy carbon electrode (0.2463 cm^2, Pine Instruments), resulting in a loading of 800 µg cm^{-2}. The working electrode with the deposited catalyst layer was used in a three-electrode cell set-up connected to a bipotentiostat (Biologic SP 300) and rotator (Pine Instruments). A graphite rod and RHE were used as counter and reference electrodes, respectively. The ORR performance was evaluated via steady-state RDE polarization in O_2-saturated 0.5 M H_2SO_4 using a rotation rate of 900 r.p.m., 20 mV potential steps from 0.05 to 0.95 V and a 25 s potential hold time at each step at room temperature, except for that during nitrite stripping. The CV was carried out between 0.05 to 0.95 V versus the RHE with a scan rate of 10 mV s^{-1} in Ar-saturated 0.5 M H_2SO_4 electrolyte. The ORR polarization curves during nitrite stripping were corrected by the CV data obtained by scanning the same electrode within the same potential range and same scan rate in Ar-saturated 0.5 M H_2SO_4 electrolyte.

In situ nitrite stripping. Measurements were conducted on a typical three-electrode cell. A 0.2463 cm^2 glassy carbon electrode with 0.27 mg cm^{-2} catalyst was used as the working electrode. A graphite rod and Ag/AgCl electrode were used as the counter and reference electrodes, respectively. Pt wire was used to correct the Ag/AgCl scale to the RHE scale. A 0.5 M acetate buffer of pH 5.2 was prepared from sodium acetate (99%, Sigma-Aldrich) and glacial acetic acid (99.8%, Sigma-Aldrich). The experimental procedures, including protocols of cleaning, measurement, poisoning and recovering, as well as catalyst loading, followed the previous report by Malko et al.[22], summarized as follows: (1) In brief, in order to clean the working electrode, the working electrode was subjected to potential cycling from 1.05 V to −0.4 V with scan rates of 100 mV s^{-1} and 10 mV s^{-1} in Ar-saturated electrolyte (20 cycles). This was repeated until reaching steady-state CV data. (2) ORR performance (unpoisoned; 1.0 V to 0.3 V) was measured in O_2-saturated electrolyte using a rotation rate of 900 r.p.m. and scan rate of 10 mV s^{-1} followed by acquisition of a CV image in Ar-saturated electrolyte between 1.0 V and 0.3 V, which was used to correct the ORR performance. Afterward, the baseline CV image was collected between 0.4 V and −0.3 V at 10 mV s^{-1}. (3) The

working electrode was immersed in 0.125 M $NaNO_2$ solution (Sigma-Aldrich) with a rotation rate of 300 r.p.m. for 5 min at the open-circuit voltage. The working electrode was washed with deionized water (1 min), electrolyte (5 min) and deionized water (1 min) using a rotation rate of 300 r.p.m. (4) The poisoned ORR performance, CV curves for ORR performance correction and stripping CV were recorded in sequence with the same parameters as in step (2). Step (4) was repeated to confirm the ORR performance and CV recovery.

Nitric oxide stripping. RDE experiments were performed with the NO-treated FeNC-CVD-750 catalyst with a catalyst loading of 600 µg cm^{-2} using a 5.5-mm-diameter glassy carbon disc and platinum ring electrode. NO treatment was conducted by exposing the catalyst powder in an alumina boat in a gas-tight stainless-steel tube to 100% NO (AirGas) for three hours at room temperature. A catalyst–ionomer ink was prepared from the NO-treated catalyst, as described above for the RDE experiments, and the ink was deposited on the glassy carbon electrode of an RDE. The NO stripping charge was determined by subtracting the steady-state negative-going voltammogram over the potential range of 0.5 to −0.2 V versus a RHE from the first negative-going voltammogram scan taken from the unpoisoned electrode. The stripping charge was converted to the number of NO molecules adsorbed by Fe–N_4 sites (Supplementary Note 5).

Electrochemical characterization—fuel cell. The FeNC-CVD-750 catalyst was used to prepare the cathode for MEA tests in a PEMFC under H_2–O_2 and H_2–air conditions. The cathode catalyst inks were prepared by dispersing a calculated amount of catalyst powder and Nafion D521 dispersion (Ion Power) into 50 wt% 1-propanol aqueous solution for 3 h under ice bath sonication. The inks were coated layer by layer on SGL 29-BC gas diffusion layer (Sigracet) until 6 mg cm^{-2} loading was achieved. The thickness of the electrode was ~180 µm, as measured by a thickness gauge (Mitutoyo, 547–526S). A commercial Pt gas diffusion electrode (0.3 mg$_{Pt}$ cm^{-2}, Fuel Cell Store) was used as the anode. The anode electrode was first hot-pressed onto an NR212 membrane (Ion Power) at 130 °C for 4 min. Before hot-pressing the cathode on the opposite side of the membrane, a thin Nafion overspray layer was applied on the cathode catalyst layer to reduce the interfacial resistance. The cathode was then hot-pressed on the previously pressed half MEA at 130 °C for 2 min. The MEA was then assembled into a single cell with single-serpentine flow channels. The single cell was then evaluated in a fuel cell test station (100 W, Scribner 850e, Scribner Associates). The cells were conditioned under a N_2 environment at 100% relative humidity and 80 °C for 2 h. Oxygen flowing at 1,000 ml min^{-1} and H_2 (purity 99.999%) flowing at 200 ml min^{-1} were used as the cathode and anode reactants, respectively. The back pressures during the fuel cell tests were 1.0 bar reactant gas. The vapour pressure was around 0.5 bar due to the 100% relative humidity. Thus, the total pressure applied to the MEA was around 1.5 bar (150 KPa). Fuel cell polarization curves were recorded in a voltage control mode.

The H_2–air performance of FeNC-CVD-750 was evaluated on the same MEA that underwent the H_2–O_2 PEMFC testing. The protocol is the same as that applied for the H_2–O_2 PEMFC evaluation except that air flowing at 2,000 ml min^{-1} and H_2 (purity 99.999%) flowing at 500 ml min^{-1} were used as the cathode and anode reactants, respectively.

Physical characterizations. *Inductively coupled plasma atomic emission spectroscopy.* Inductively coupled plasma atomic emission spectroscopy tests were conducted at Robertson Microlit Laboratories.

TEM. The TEM image of the ZIF-8 was recorded with a JEOL 2010 field emission gun.

STEM. AC-STEM was conducted using a JEOL NEOARM TEM/STEM operated at 80 keV and equipped with a Gatan Quantum electron energy-loss spectrometer and dual 100 m^2 silicon drift detectors for energy dispersive X-ray spectroscopy.

SEM. SEM micrographs of Zn–N–C were obtained with a Hitachi S-4800 apparatus.

X-ray diffraction. X-ray diffraction patterns were conducted using a PANanalytical X'Pert Pro powder X-ray diffractometer with Cu Kα radiation.

XPS. XPS tests were done with Kratos AXIS Ultra DLD spectrometer with an Al Kα (1,486.6 eV) X-ray source at the University of California, Los Angeles.

N_2 adsorption/desorption analysis. N_2 sorption analysis was performed at liquid nitrogen temperature (77 K) with a Micromeritics ASAP 2020 instrument. Prior to the measurements, all samples were degassed at 200 °C for 5 h in flowing nitrogen to remove guest molecules or moisture. The pore size distributions were calculated by fitting the full isotherm with the quench solid density functional theory model with slit pore geometry from NovaWin (Quantachrome Instruments).

Mössbauer spectroscopy. The ^{57}Fe Mössbauer spectroscopy was used to obtain information on iron speciation. Samples of ~300 mg were mounted in a 2 cm^2

holder. Mössbauer spectra were measured at 5 K in a helium flow cryostat (SHI-850 Series from Janis). The Mössbauer spectrometer (Wissel) was operated in transmission mode with a ^{57}Co:Rh source at room temperature. The velocity driver was operated in constant acceleration mode with a triangular velocity waveform. The velocity scale was calibrated with the magnetically split sextet of a high-purity α-Fe foil at room temperature. The spectra were fitted to appropriate combinations of Lorentzian profiles representing quadrupole doublets and sextets by least-squares methods. Isomer shifts are given relative to α-Fe at room temperature.

X-ray absorption spectroscopy (XAS) measurements. The ex situ XAS measurements at the Zn K edge of Zn(II)Pc, ZIF-8 and Zn–N–C were performed in transmission mode at beamline 10-ID of the Materials Research Collaborative Access Team at the Advanced Photon Source, Argonne National Laboratory. Ex situ XAS measurements at the Fe K edge of Fe-based catalysts were conducted at beamline ISS 6-BM and 8-ID in fluorescence mode of the National Synchrotron Light Source II (Brookhaven National Laboratory). In addition, in situ XAS measurements were conducted on FeNC-CVD-750. The ink for the XAS electrode was composed of 1:3 (wt%), 18.2-MΩ-purity deionized water (Millipore) and 2-propanol (HPLC-grade, Aldrich), a 5 wt% Nafion solution (Aldrich) and FeNC-CVD-750 catalyst powder. The inks were directly sprayed onto a Zoltek carbon cloth on a piece of heated glass. The final Fe loading was ~0.05 mg$_{Fe}$ cm^{-2} in the electrodes (1 × 3 cm^2). Ex situ XAS data were first collected on the dry electrode, which was then conditioned in 0.5 M H$_2$SO$_4$ under vacuum for three hours to remove the oxides, impurities and gases trapped inside the electrode, and to thoroughly wet the electrodes. Afterward, the electrode was mounted onto an electrochemical half-cell reported previously[49] and further conditioned electrochemically for 50 cycles between 0.05 and 0.95 V with a scan rate of 50 mV s^{-1} in N$_2$-saturated 0.5 M H$_2$SO$_4$ electrolyte. Full range Fe K-edge spectra were taken at various static potentials along the anodic sweep of the CV in O$_2$-saturated 0.5 M H$_2$SO$_4$ electrolyte. Data were collected in fluorescence mode with an Fe reference foil positioned between the two ionization chamber detectors I2 and I3 as a reference. The voltage cycling limits were 0.50 to 0.95 V versus RHE. The XAS data were processed and fitted using the IFEFFIT-based Athena and Artemis programs[50]. Scans were calibrated, aligned and normalized with background removed using the IFEFFIT suite[50]. The χ(R) were modelled using single scattering paths calculated by FEFF6 (ref. [51]).

Temperature-programmed reaction. Temperature-programmed reaction studies were performed using an Altamira (AMI-100) system equipped with a residual gas analyser QMS200 (Stanford Research Systems). The temperature-programmed reaction profile was obtained by flowing 5 ml min^{-1} He through sequential beds of 26 or 30 mg anhydrous ferric chloride and 26 or 30 mg of Zn–N–C while ramping the temperature from room temperature to 775 °C at a rate of 5 °C min^{-1} or from room temperature to 880 °C at a rate of 25 °C min^{-1}. The temperature was then held for 3 h. Mass to charge (*m/z*) ratios of 32, 35, 36, 126, 136 and 161 were monitored with the residual gas analyser, corresponding to O$_2$, Cl, HCl, FeCl$_2$, ZnCl$_2$ and FeCl$_3$, respectively.

Data availability
The data supporting the findings of this study are available within this Article and its Supplementary Information. Additional data are available from the corresponding authors upon reasonable request. Source data are provided with this paper.

References

49. Jia, Q. et al. Activity descriptor identification for oxygen reduction on platinum-based bimetallic nanoparticles: *in situ* observation of the linear composition–strain–activity relationship. *ACS Nano* **9**, 387–400 (2015).
50. Newville, M. IFEFFIT: interactive XAFS analysis and FEFF fitting. *J. Synchrotron Radiat.* **8**, 322–324 (2001).
51. Ankudinov, A. L., Ravel, B., Rehr, J. J. & Conradson, S. D. Real-space multiple-scattering calculation and interpretation of X-ray-absorption near-edge structure. *Phys. Rev. B* **58**, 7565–7576 (1998).

Author contributions
Q.J., D.J.M. and F.J. conceived the project. Q.J. and J.L. conceived and designed the CVD method. Q.J., J.L., D.J.M., F.J. and L.J. developed the CVD method. L.J. synthesized the FeNC-CVD-T catalysts; Q.J. and S.M. supervised and advised the synthesis. L.J. conducted the RDE, Brunauer–Emmett–Teller, X-ray diffraction, TEM, SEM and inductively coupled plasma atomic emission spectroscopy. L.J., Q.S., L.L.R., T.S., E.L. and Q.J. conducted the XAS on the FeNC-CVD-750. T.S. and D.J.M. conducted the XAS on the Zn–N–C and ZIF-8 at the Zn K edge. Q.J. analysed the XAS data. M.T.S., J.L. and F.J. conducted the Mössbauer and the fitting. Z.Z. and Y.H. conducted the XPS and fitting. F.Y., S.Z. and H.X. conducted the PEMFC operation and data analysis. D.A.C. conducted the ADF-STEM, electron energy-loss spectroscopy and data analysis. M.F. and D.J.M. conducted the temperature-programmed reaction studies. J.H.P., M.F. and D.J.M. conducted the NO stripping and data analysis. L.J. did the nitrite stripping. Q.J., F.J., D.J.M. and L.J. wrote the manuscript and prepared the figures.

Competing interests
L.J., S.M. and Q.J. have filed a full patent application (no. PCT/US2020/058362) based on the results of this manuscript. The inventors are Q.J., L.J., and S.M. The application is currently pending. The CVD method for the synthesis of M–N–C catalysts is covered by this patent application. The remaining authors declare no competing interests.

Additional information
Supplementary information The online version contains supplementary material available at https://doi.org/10.1038/s41563-021-01030-2.

Correspondence and requests for materials should be addressed to D.J.M., F.J. or Q.J.

Peer review information *Nature Materials* thanks the anonymous reviewers for their contribution to the peer review of this work.

Reprints and permissions information is available at www.nature.com/reprints.